remote sensing

MDPI

Article

Near-Real Prediction of Earthquake-Triggered Landslides on the Southeastern Margin of the Tibetan Plateau

Aomei Zhang [1], Xianmin Wang [1,2,3,4,*], Chong Xu [5,6], Qiyuan Yang [1], Haixiang Guo [4] and Dongdong Li [7]

[1] Hubei Subsurface Multi-Scale Imaging Key Laboratory, School of Geophysics and Geomatics, China University of Geosciences, Wuhan 430074, China; zgdzdxzam@cug.edu.cn (A.Z.)
[2] State Key Laboratory of Biogeology and Environmental Geology, China University of Geosciences, Wuhan 430074, China
[3] Key Laboratory of Geological and Evaluation of Ministry of Education, China University of Geosciences, Wuhan 430074, China
[4] Laboratory of Natural Disaster Risk Prevention and Emergency Management, School of Economics and Management, China University of Geosciences, Wuhan 430074, China
[5] National Institute of Natural Hazards, Ministry of Emergency Management of China, Beijing 100085, China; xuchong@ies.ac.cn
[6] Key Laboratory of Compound and Chained Natural Hazards Dynamics, Ministry of Emergency Management of China, Beijing 100085, China
[7] College of Electronic Science and Engineering, National University of Defense Technology, Changsha 410073, China
* Correspondence: wangxianmin@cug.edu.cn

Abstract: Earthquake-triggered landslides (ETLs) feature large quantities, extensive distributions, and enormous losses to human lives and critical infrastructures. Near-real spatial prediction of ETLs can rapidly predict the locations of coseismic landslides just after a violent earthquake and is a vital technical support for emergency response. However, near-real prediction of ETLs has always been a great challenge with relatively low accuracy. This work proposes an ensemble prediction model of EnPr by integrating machine learning tree models and a deep learning convolutional neural network. EnPr exhibits relatively strong prediction and generalization performance and achieves relatively accurate prediction of ETLs. Six great seismic events occurring from 2008 to 2022 on the southeastern margin of the Tibetan Plateau are selected to conduct ETL prediction. In a chronological order, the 2008 M_s 8.0 Wenchuan, 2010 M_s 7.1 Yushu, 2013 M_s 7.0 Lushan, and 2014 M_s 6.5 Ludian earthquakes are employed for model training and learning. The 2017 M_s 7.0 Jiuzhaigou and 2022 M_s 6.1 Lushan earthquakes are adopted for ETL prediction. The prediction accuracy merits of ACC and AUC attain 91.28% and 0.85, respectively, for the Jiuzhaigou earthquake. The values of ACC and AUC achieve 93.78% and 0.88, respectively, for the Lushan earthquake. The proposed EnPr algorithm outperforms the algorithms of XGBoost, random forest (RF), extremely randomized trees (ET), convolutional neural network (CNN), and Transformer. Moreover, this work reveals that seismic intensity, high and steep relief, pre-seismic fault tectonics, and pre-earthquake road construction have played significant roles in coseismic landslide occurrence and distribution. The EnPr model uses globally accessible open datasets and can therefore be used worldwide for new large seismic events in the future.

Keywords: Tibetan Plateau; coseismic landslide; near-real-time; ensemble learning

Citation: Zhang, A.; Wang, X.; Xu, C.; Yang, Q.; Guo, H.; Li, D. Near-Real Prediction of Earthquake-Triggered Landslides on the Southeastern Margin of the Tibetan Plateau. *Remote Sens.* **2024**, *16*, 1683. https://doi.org/10.3390/rs16101683

Academic Editor: Michele Saroli

Received: 22 April 2024
Revised: 6 May 2024
Accepted: 7 May 2024
Published: 9 May 2024

1. Introduction

Earthquake-triggered landslides (ETLs) are a representative type of secondary hazard caused by earthquakes and feature huge quantities, wide distribution, sudden onset, and great destructiveness [1]. For example, a total of 197,481 landslides were triggered by the Wenchuan earthquake on 12 May 2008, and they were widely distributed over an area

of 75,424 km² [2]. These coseismic landslides brought a huge loss to human lives and properties by severely blocking traffic, destroying buildings, and causing dammed lakes. The ETLs also posed a great challenge to emergency rescue. Earthquakes have occurred frequently in recent years due to crustal movement. Co-seismic landslides are usually accompanied by large numbers of casualties. According to the Wenchuan Earthquake Rescue Committee, there were more than 80,000 casualties of the earthquake, of which about 30,000 resulted from the ETLs [2]. Therefore, rapid prediction of ETL positions just after a violent earthquake, i.e., near-real-time prediction of coseismic landslides, is very crucial for effective and efficient emergency rescue.

Remote sensing images are extensively employed in ETL recognition [3]; however, they cannot meet the high timeliness demand in emergency rescue. (1) The lack of images for the extensive earthquake-struck region after a great earthquake and dense cloud coverage in images may both result in missing recognition of numerous landslides. For example, almost half of coseismic landslides (about 5000 landslides) triggered by the 2022 Luding earthquake cannot be interpreted due to dense cloud cover on the post-earthquake optical satellite images [4]. (2) The quality of optical remote sensing images is seriously constrained by weather conditions [5]. The wide coverage of fog and clouds significantly impede the identification of ETLs. Continuous cloud cover during a single monsoon season typically persists for several months, e.g., from May to September [6]. (3) The complete interpretation of large quantities of coseismic landslides may cost weeks to months. For example, the 2015 Gorkha (Nepal) earthquake triggered around 24,903 landslides covering more than 30,000 km² [7]; thus, it was very time-consuming to interpret landslides over such an extensive region. As a contrast, near-real prediction of ETLs only requires hours after a violent earthquake.

The current models for near-real ETL prediction mainly include two types: physical models and statistical models. (1) Physical models are established according to landslide movement mechanisms. This type of model employs the Newmark method [8] and calculates landslide probability and displacement in terms of the slope properties and ground motion parameters provided by the United States Geological Survey (USGS) ShakeMap [9]. Godt et al. [10] proposed a hybrid method combining a simplified Newmark [8] stability analysis and heuristic models to predict the ETL distribution in a spatial resolution of 1 km. Cheng et al. [11] used the Newmark sliding-block method and ground motion parameters for near-real EQIL prediction in a spatial resolution of 160 m. The intersection over union (IoU) value attained 11.65% and was higher than the ones of the PAGER method [12] and Godt model [10]. Physical models can achieve relatively high accuracy with precise geotechnical and ground motion parameters. However, in large earthquake zones, obtaining precise geotechnical parameters is difficult, constraining the accuracy and applicability of physical models. (2) Statistical models include fuzzy logic-based statistical models and landslide inventory-based statistical models. Fuzzy logic-based statistical models employ fuzzy logic models to depict the relation between various prediction indices and landslide probability. Then, they predict ETL distribution based on the established relationship [13,14]. Robinson et al. [15] proposed a fuzzy logic method to determine the landslide-inducing factors and to predict the spatial probability of coseismic landslides according to some landslides occurring shortly after the earthquake. Landslide inventory-based statistical models predict the ETL distribution of an earthquake in terms of the coseismic landslide data from other historical earthquake events [1,12,16]. The most representative method is the Global Rapid Assessment for Earthquake Response, PAGER [12]. Nowicki et al. [17] developed a logistic regression (LR)-based statistical model from five ETL inventories, and the spatial resolution of the predicted ETL distribution is 1 km. He et al. [18] established a global model for rapid evaluation of ETL spatial distribution by the random forest (RF) algorithm. The model was trained via 288,114 landslides from 16 high-quality ETL inventories, and the predicted area under curve (AUC) values were 0.873, 0.907, and 0.786, respectively, for the 1989 Loma Prieta, 2013 Lushan, and 2016 Kaikoura earthquakes.

Substantial advancements have been made in ETL prediction; however, there are still some challenges. (1) Physical models require geotechnical data, but accurate geotechnical parameters are difficult to obtain in most regions of the world [12]. That has constrained the application and promotion of physical models. (2) ETL-prediction machine learning algorithms feature relatively high false alarms, low generalization performance, and low accuracy. (3) ETL-prediction deep learning algorithms are heavily dependent on data quantities. Their strong learning ability and high accuracy demand massive data and complicated structures.

Regarding physical models, the geological parameters, such as unit weight, effective friction angle, and effective cohesion, in a vast geographical area are challenging to determine. Existing methods for determining geological parameters include field surveys and predictions based on landslide inventories [19]. In post-earthquake emergencies, it is impractical to investigate field studies of geological parameters in large-scale areas. Predictions using historical landslide inventories and the Newmark displacement model require assumptions about a number of parameters and rely on historical statistics. Regarding the machine learning algorithms, machine learning models such as RF, LR, etc., are often accompanied by relatively high false alarms, low generalization performance, and low accuracy [20] when ETL predictions are required for large-scale and geographically complex areas. In addition, the deep learning is highly data-dependent, and the larger the amount of data, the better the performance.

Focusing on the above challenges, this work makes two contributions. (1) The globally available data of topography, geology, geography, and earthquakes are employed to conduct near-real ETL prediction. These data can be acquired worldwide before an earthquake or within minutes after an earthquake; thus, this work can be applied to any future earthquake in the world. (2) A novel EnPr model is proposed to integrate decision tree structures and a convolutional neural network (CNN) architecture. The EnPr model combines the advantages of machine learning and deep learning and is characterized by relatively high accuracy, good generalization, and a simple structure. It can achieve a good learning ability based on a relatively small data set.

This study centers around the seismic events that took place on the southeastern boundary of the Tibetan Plateau between 2008 and 2022 (Table 1). Its main objective is to conduct near-real-time prediction of ETL distributions. The four earthquakes occurring from 2008 to 2014 (the 2008 M_s 8.0 Wenchuan, 2010 M_s 7.1 Yushu, 2013 M_s 7.0 Lushan, and 2014 M_s 6.5 Ludian earthquakes) are used to train and build the EnPr model. The two earthquakes occurring from 2017 to 2022 (the 2017 M_s 7.0 Jiuzhaigou and 2022 M_s 6.1 Lushan earthquakes) are selected for ETL prediction in order to assess the reliability and accuracy of the EnPr model. Furthermore, this work reveals the key geoenvironmental and disaster-inducing factors closely relevant to the occurrence and distribution of coseismic landslides in the Tibetan Plateau.

Table 1. Six violent earthquakes studied in this work.

ID	Location	Date	Magnitude (M_s)	Number of Landslides	Survey Area (km²)	Reference
1	Wenchuan	12 May 2008	8.0	197,481	116,835.9	Xu et al. (2014) [2]
2	Yushu	13 April 2010	7.1	2036	8573.4	Xu et al. (2013) [21]
3	Lushan	20 April 2013	7.0	15,546	7202.0	Xu et al. (2015) [22]
4	Ludian	3 August 2014	6.5	1024	290.7	Xu et al. (2014) [23]
5	Jiuzhaigou	8 August 2017	7.0	5563	859.8	Wang et al. (2022) [24]
6	Lushan	1 June 2022	6.1	2352	12,174.5	Shao et al. (2022) [25]

2. Study Area and Multisource Data

2.1. Study Area

The study area (Figure 1) is located in the seismically active region on the southeast edge of the Tibetan Plateau.

The convergence of the Indian and Eurasian plates, which occurred 50 Ma ago, led to the rapid uplift of the Tibetan Plateau and the shortening of the crust within the suture zone by at least 1500 km [26]. As a result of the successive land–land collisions between the Indian subcontinent and the southern part of the Eurasian continent, the Yarlung Zangbo river suture belt was formed. This resulted in the long-term southeastward escape of materials from the eastern edge of the Tibetan Plateau and a strong neotectonic movement [27]. The southeastern margin of the Tibetan Plateau may have experienced three stages of regional tectonic deformation during the Cenozoic [28]. The Eocene-Early Oligocene crust shortened and thickened in response to early Indo-Asian continental convergence, leading to regional metamorphism and deep melting [28]. Three continental-scale shear zones began to slip-shear simultaneously in the Late Oligocene, accompanied by block extrusion. They may have been corridors for vertical extrusion of low-viscosity lower and middle crustal materials [28]. In the middle-late Miocene, the deformation type and slip reversal of the major fracture systems changed significantly along the southeastern margin of the Tibetan Plateau [28].

After the occurrence of the Wenchuan earthquake in 2008, several moderate to severe earthquakes took place in the study area. Their seismogenic faults are secondary active faults near the main boundary faults of the Grade I and II active blocks [22]. Thus, the stress has accumulated to a high level in the main boundary faults on the eastern and southeastern edges of the Tibetan Plateau [29]. The 2008 Wenchuan, 2013 Lushan, and 2022 Lushan earthquakes occurred in the northeast-trending Longmenshan fault zone. The Xianshuihe fault zone, northwest-oriented Ganzi fault, Yushu fault, Batang fault, Dangjiang fault, south-oriented Anninghe fault, Zemuhe fault, and Xiaojiang fault constitute a huge left-slip fault system (called the Xianshuihe fault zone system) [4]. This fault zone system forms the eastern boundary of the Sichuan–Yunnan rhombic block [4]. The 2014 Ludian earthquake occurred in the boundary deformation zone between the Sichuan–Yunnan rhombic block and the South China land mass. The 2017 Jiuzhaigou earthquake was located at the northern section of the Huya fault that is one of the eastern branch faults of the East Kunlun fault zone [29]. The 2010 Yushu earthquake was situated at the Garzê–Yushu fault that is a sinistral strike-slip fault on the western segment of the Xianshuihe fault zone [30].

Due to the uplift of the Tibetan Plateau, the plateau materials have been consistently shifted towards the southeast direction. This geological process has resulted in higher terrains in the northern regions and lower terrains in the southern areas of Tibetan Plateau [31,32]. The relief is steep in the study area and characterized by mountains and plateaus. The three primary rivers of Salween, Mekong, and Yangtze flow southward along the southeastern edge of the plateau and constitute dense river networks [21]. Human engineering activities are frequent in the low and middle elevation areas, including house construction, animal grazing, and engineering excavation.

Therefore, the study area is one of the most ETL-frequent regions worldwide because of concentrated fault zones, active tectonic movement, frequent seismic activities, steep relief, dense water systems, and intensive human engineering activities.

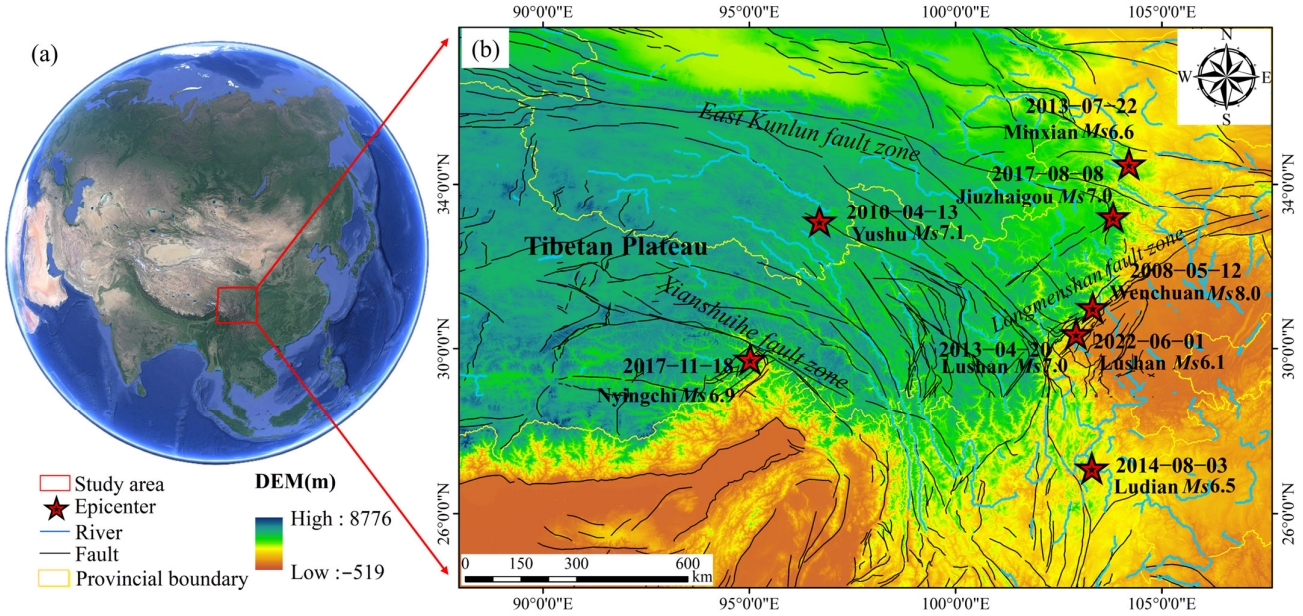

Figure 1. Seismic and tectonic characteristics in the study area. (**a**) Location of the study area in Eurasia. The Earth picture is sourced from Google Earth accessed on 2 May 2023. (**b**) Topographic features, fault distribution, river networks, and recently occurring catastrophic earthquakes in the study area.

2.2. Multisource Data

Five sets of multi-source data (Table 2) are utilized to predict the spatial distribution of landslides triggered by earthquakes. (1) SRTM DEM data are used to construct the topographic factors of elevation, slope angle, aspect, plan curvature, and profile curvature. (2) The geological fault data are adopted to build the geological factors of distance to fault and fault kernel density. (3) The land use data reflect the characteristics and types of human engineering activities, and the road network data is utilized to construct the human activity factor of distance to road. (4) The river network data are employed to establish the environmental factor of distance to river. (5) The ShakeMap data are adopted to establish the seismic factors of PGV, peak ground acceleration (PGA), Modified Mercalli Intensity (MMI), and distance to the epicenters of these earthquakes.

Table 2. Multisource data employed in this work. USGS: United States Geological Survey; CENC: China Earthquake Networks Center; SRTM: Shuttle Radar Topography Mission; and DEM: Digital Elevation Model.

Data type	Data	Date	Resolution	Source
Terrain	SRTM DEM	2000	30 m	Geospatial Data Cloud v4.1
Geology	Geological fault	Pre-earthquake	—	Styron et al. 2020 [33]; Wang, L. 2021 [34]; Li et al. 2017 [35]
Human activity	Land use	Pre-earthquake	30 m	GLOBELAND30
	Road Network	Pre-earthquake	—	OpenStreetMap v1.0.0; Google earth v7.3
Environment	River network	Pre-earthquake	—	OpenStreetMap v1.0.0; Google earth v7.3
Seismology	Earthquake inventory	2008, 2010, 2013, 2014, 2017, 2022	—	USGS CENC

3. Methodology

Figure 2 shows the technical route for near-real-time prediction of ETLs, and it consists of five main steps. (1) The geoenvironmental and disaster-inducing factors are extracted from the multisource data to establish prediction indices. (2) The study area is segmented into slope units by a surface curvature watershed method. Slope units can well portray the topographic constraint to landslide occurrence, reflect the control of water systems to landslide development, and avoid meaningless fragmented patches in the prediction result. Thus, the utilization of slope units can effectively improve ETL prediction accuracy. (3) Four earthquakes—2008 M_s 8.0 Wenchuan, 2010 M_s 7.1 Yushu, 2013 M_s 7.0 Lushan, and 2014 M_s 6.5 Ludian—are employed to construct and train the EnPr model. (4) The EnPr model is used to predict the ETL distribution of two earthquakes: 2017 M_s 7.0 Jiuzhaigou and 2022 M_s 6.1 Lushan. All actual coseismic landslides induced by the two earthquakes are adopted to validate the accuracy of the EnPr model. (5) The EnPr model is compared with the RF, extremely randomized trees (ET), XGBoost (1.6.2), CNN, and Transformer models to demonstrate its performance superiority.

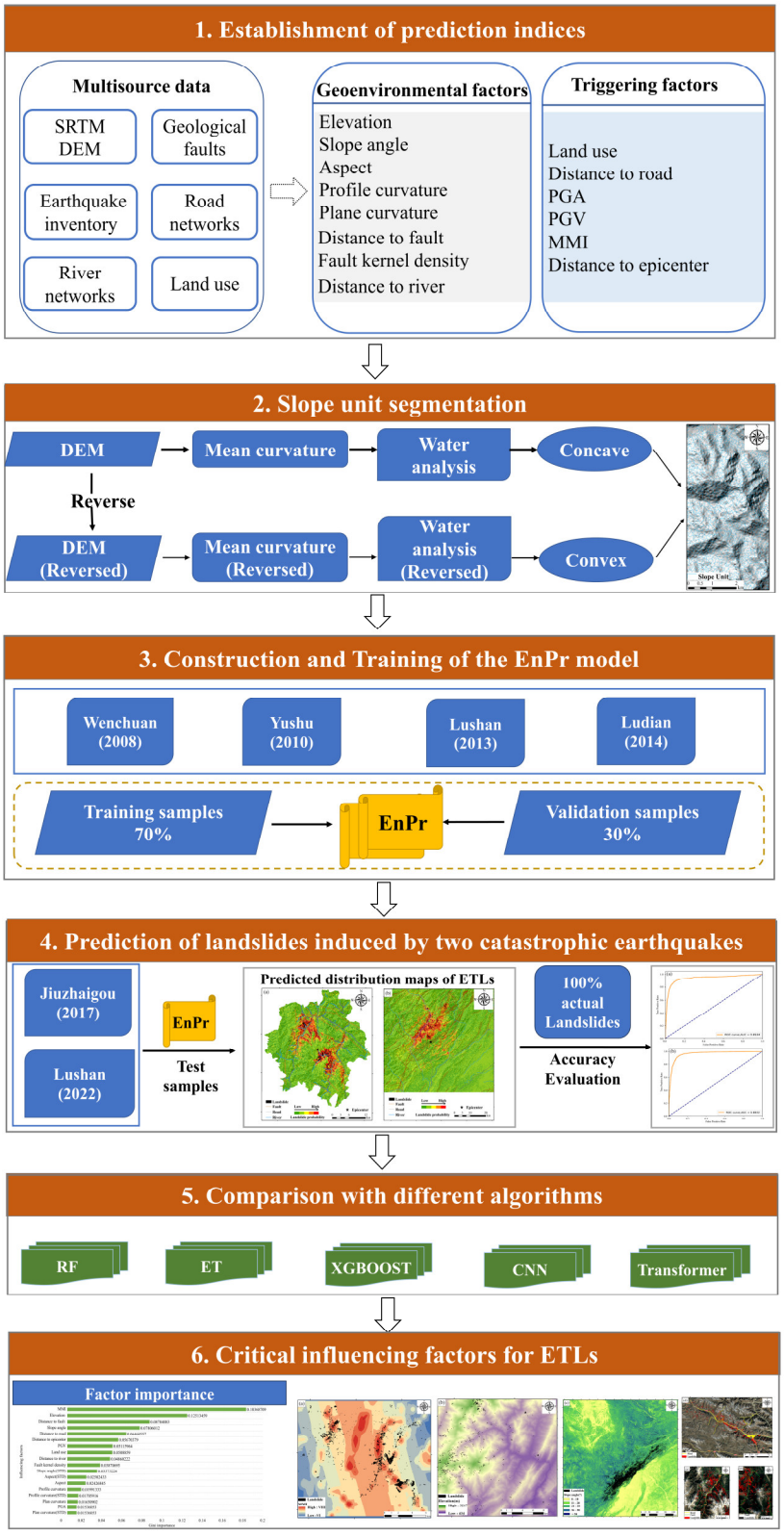

Figure 2. Technical route for near-real spatial prediction of coseismic landslides. PGV: peak ground velocity; PGA: peak ground acceleration; MMI: modified Mercalli intensity; ETLs: earthquake-triggered landslides; RF: random forest; ET: extremely randomized trees; XGBoost: eXtremeGradient Boosting; CNN: convolutional neural network.

3.1. Establishment of Prediction Indices

There are two types of factors affecting the distribution of ETLs: geoenvironmental factors and triggering factors. Geoenvironmental factors control the development of coseismic landslides, and triggering factors induce the occurrence of coseismic landslides. The established influencing factors are shown in Table 3 and constitute the prediction indices of ETLs. The geoenvironmental factors include the geological and topographical factors. (1) In terms of geology, fault tectonics damage the adjacent rock and soil mass. Thus, the factors of fault density and distance to faults reflect the destruction to slope materials and the development of cracks within rock and soil mass. In addition, the densely distributed cracks near faults create flow channels for rainwater and underground water. The slope stability decreases under the softening and soaking of water to soil and rock mass [36]; thus, it is apt to evolve into a landslide in a great earthquake. (2) Regarding topography, elevation is closely relevant to vegetation growth, soil moisture, and human engineering activities, and these factors play a significant role in slope stability. Moreover, coseismic landslides usually occur on narrow ridges, which embody the amplification action of high slopes to seismic waves [37]. Due to significant seismic amplification effects and long-term exposure to weathering and distress on the high slope, the pore structure of the upper slope soil is initially disrupted, resulting in scattered seismic subsidence of the upper soil and the formation of tensile cracks in the rear part of the slope [37]. In gently sloping terrain like ridges and terraces, the middle and lower parts of the soil undergo short-distance shearing and sliding due to the additional loading from the subsided upper soil and the combined action of seismic inertia forces, forming a slump-type seismic subsidence landslide [37]. On steep slopes such as edges of plateaus, terraces, and valley slopes, the subsided soil at the upper part directly collapses and forms a rockslide-type seismic subsidence landslide [37]. Slope angle indicates the steep free surfaces and geopotential energy of a slope [38]. Also, steep relief can amplify the reflection and refraction of seismic waves and intensify the damage of seismic waves on rock and soil mass [39]. Thus, high and steep slopes tend to lose stability and run out during a large earthquake. Aspect reflects the solar radiation on a slope and is closely related to vegetation coverage and soil saturation, which obviously affect the stability of a slope. Furthermore, fault strike and rupture direction determine the aspect featuring abundant coseismic landslides. Profile curvature and Plane curvature illuminate the surface relief that controls the stress distribution within a slope and the runoff velocity along the slope surface [39]. The slopes with large internal stress and strong runoff scouring are inclined to lose stability and develop into landslides when suffering from an earthquake. The factor of distance to rivers indicates the disruption of slope stress balance by river erosion and undercutting. Additionally, the significant fluctuations in river levels resulting from an earthquake may elevate the hydrodynamic pressure within the slope adjacent to the river, thereby causing instability in the slope [9]. Under the action of seismic forces, the pore pressure in saturated soil increases while the effective stress decreases, leading to liquefaction of the soil on slopes. Instantaneous water film formed between the liquefied soil layer itself or between the liquefied soil layer and the underlying impermeable layer creates a sliding surface. If the liquefied layer is located at the bottom of the slope, it often triggers long-distance sliding of the overlying unsaturated soil. When the liquefied layer is situated at the surface of the slope, it induces long-distance earthflows along the slope surface. In cases where liquefaction occurs at both the bottom and the surface of the slope, sliding of the soil above the liquefied bottom layer and surface earthflows can happen simultaneously [40]. Therefore, the slopes suffering from river erosion may gradually become instable and tend to fail during an earthquake.

The disaster-triggering factors involve the seismic and human engineering activity factors. (1) As for earthquakes, the factors of PGA and PGV reflect the propagation of seismic waves, and the factors of MMI and distance to the epicenter embody the strength and intensity of ground motion. Thus, the seismic factors illuminate the destruction of seismic waves to the ground and slope surfaces [41]. (2) As to human engineering activities, the

factor of distance to roads indicates the excavation to slope feet and the damage to rock and soil intactness. The stress redistribution within a slope may change the seepage field and generate new seepage channels. The infiltrated rainwater aggregates on the impervious surface, saturates rock and soil mass, and softens the sliding surface [42]. Therefore, the slopes beside roads are apt to fail and evolve into landslides under the function of express pore water pressure when suffering from a violent earthquake. The factor of land use depicts the intensification and types of human engineering activities before an earthquake. The artificial excavation [43–45] and explosion in urban construction cause plenty of cracks within a slope, and the exposed debris features a strong water permeability and is easily weathered to become fractured. Moreover, cropland irrigation results in irrigation water penetrating into the soil and the increase in porewater pressure, so the shear strength of slope mass significantly reduces [42]. Therefore, the slopes undergoing intensive human engineering activities are characterized by relatively poor stability and may develop into landslides under strong earthquake ground motion.

Table 3. Geoenvironmental and triggering factors influencing coseismic landslide distribution. PGV: peak ground velocity; PGA: peak ground acceleration; and MMI: modified Mercalli intensity.

Factor Type		ID	Influencing Factor	Grade
Geoenvironmental factor	Topography	1	Elevation (m)	Continuous
		2	Slope angle (°)	Continuous
		3	Aspect	(1) Flat; (2) N; (3) NE; (4) E; (5) SE; (6) S; (7) SW; (8) W; (9) NW
		4	Plan curvature	Continuous
		5	Profile curvature	Continuous
		6	Distance to river (m)	Continuous
	Geology	7	Distance to fault (km)	Continuous
		8	Fault kernel density	Continuous
Triggering factor	Human activity	9	Land use	(1) Cultivated land; (2) Forest; (3) Grassland; (4) Shrubland; (5) Wetland; (6) Water body; (7) Tundra; (8) Artificial surface; (9) Bare land; (10) Permanent snow and ice
		10	Distance to road (m)	Continuous
	Seismology	11	PGA (g)	Continuous
		12	PGV (cm/s)	Continuous
		13	MMI	Continuous
		14	Distance to epicenter (km)	Continuous

3.2. EnPr Model for Earthquake-Induced Landslide Prediction

The structure of the EnPr model is shown in Figure 3 and contains three main steps. (1) The prediction index value vector u of each slope unit is input into the EnPr model. (2) The EnPr model involves four branches: RF, ET, XGBoost, and CNN. The vector u is input into the four branches, respectively, to output four prediction vectors: y_r, y_e, y_x, and y_c (Equation (1)). (3) The feature vectors, y_r, y_e, y_x, and y_c, are input into the XGBoost model for ensemble learning. The prediction result after ensemble learning is the occurrence probability p of coseismic landslides in each slope unit (Equation (2)). During the process of ensemble learning, a larger weight is assigned to the feature vector y that has a lower residual value (i.e., the predicted feature y is closer to the actual value).

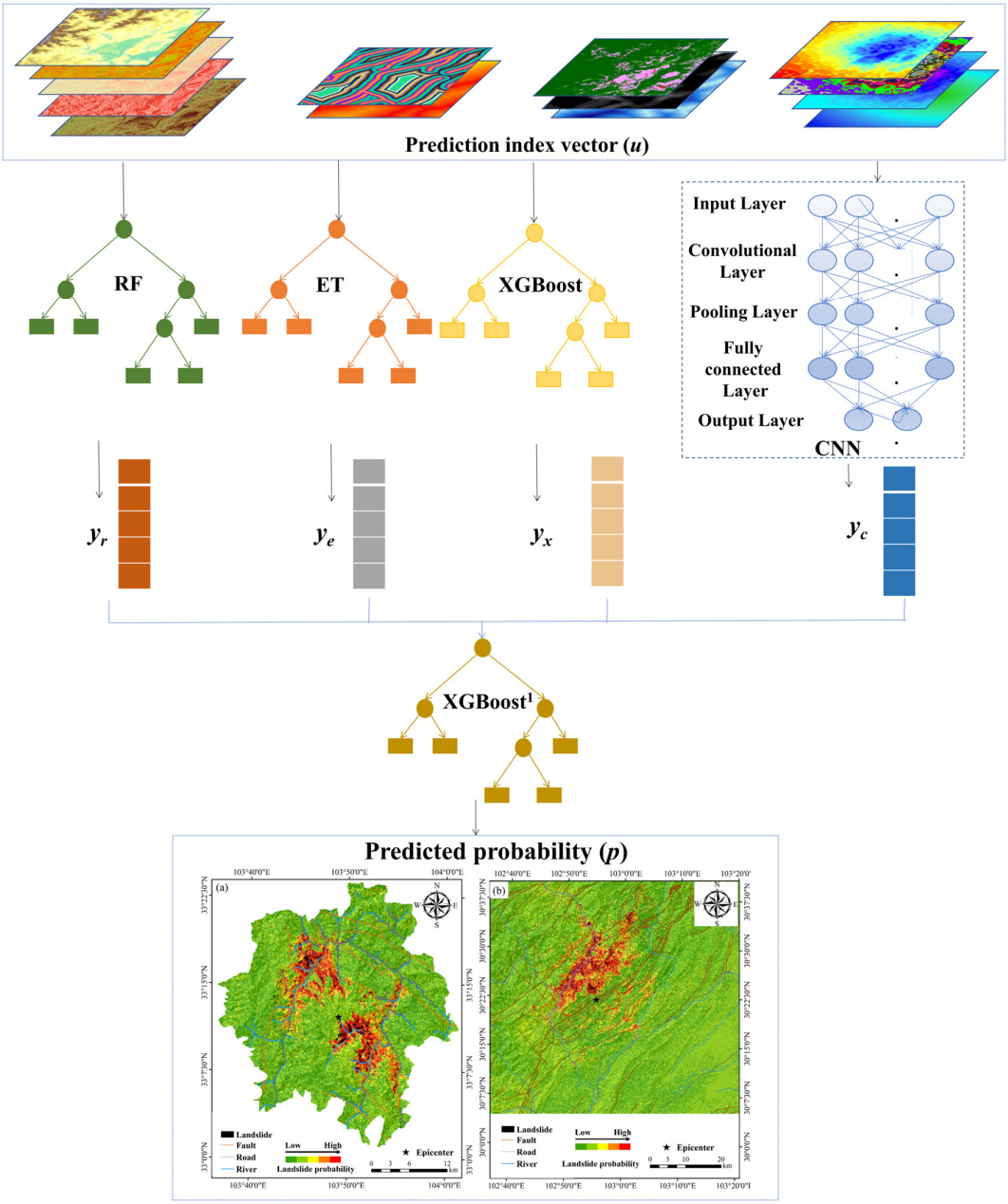

Figure 3. Architecture diagram of the suggested EnPr model. The prediction index vector u contains geoenvironmental and triggering factors. y_r, y_e, y_x, and y_c are the predicted values of the RF, ET, XGBoost, and CNN models, respectively. p is the predicted probability value of the ensemble model EnPr (i.e., XGBoost¹, this subscript 1 is to distinguish it from the previous XGBoost.). (**a**,**b**) are spatial distribution prediction of landslides triggered by the Jiuzhaigou and Lushan earthquakes, respectively.

$$y(u) = \text{model}(u) \tag{1}$$

where the function model represents the prediction model of RF, ET, XGBoost, or CNN. u is the prediction index value vector in each slope unit, and y is the predicted feature output from each model.

$$p(y) = \text{XGBoost}^1(y_r, y_e, y_x, y_c) \tag{2}$$

where p is the occurrence probability of coseismic landslides in each slope unit. y_r, y_e, y_x, y_c mean the predicted features of RF, ET, XGBoost, and CNN, respectively.

Ensemble learning can acquire a strong and optimized predictor of EnPr by integrating the advantages of the four models. Ensemble learning can effectively avoid local optimum, reduce variance, and overcome overfitting. In addition, an ensemble model is generally insensitive to abnormal data and has strong noise immunity. Thus, the EnPr model can achieve higher accuracy than each single model and possesses a good generalization performance when it is applied in the cross-region prediction.

RF [46–48] is an ensemble tree-structured algorithm, and it establishes a forest composed of uncorrelated decision trees by bagging and feature randomness. The bagging strategy trains a series of independent models by random data samples and integrates these models to yield a more accurate prediction. Bagging can effectively reduce variance within a noisy dataset. Feature randomness means each decision tree is constructed according to a random subset of features, so there is more diversity and low correlation among various decision trees. RF features two key benefits: reduced risk of overfitting and flexibility. First, a random forest involves a robust number of uncorrelated trees; thus, it can decrease the overall variance and prediction error. Second, due to feature bagging, RF can retain accuracy even if a part of the data is missing.

ET [49] is also a tree-based ensemble-learning model and integrates multiple trees to conduct prediction. Different from RF, ET trains the trees over the entire dataset by using different subset of features. ET possesses the advantages of reduction in bias and decreased variance. First, the trees are established by learning from each observation in the dataset. Different data subsets may produce varied biases, and ET samples the entire dataset, so it can effectively prevent bias. Second, a decision tree in the ET is constructed by the randomized splitting of nodes. The randomness of attributes and cutpoints can significantly lower variance. Thus, the prediction result is not obviously influenced by certain features in the dataset.

CNN [50] is a neural network and composed of an input layer, a convolutional layer, a pooling layer, a fully connected layer, and an output layer in this work. The convolution kernel in the convolution layer extracts a high-level pattern from low-level features and creates a feature hierarchy. In addition, a ReLu transformation is employed to depict the nonlinear relationship among features. The pooling layer reduces feature dimensionality and parameter number by downsampling. Thus, pooling can lower model complexity, improve efficiency, and constrain overfitting risk. The fully connected layer conducts the task of landslide probability prediction in terms of the extracted features by the previous layers. The layer leverages a Tanh activation function to produce a landslide probability y_c from 0 to 1.

XGBoost [51] leverages ensemble learning to transform a series of weak learning models to a strong and generalized model. It employs gradient augmentation and regularization to prevent overfitting. In addition, the techniques of preordering and weighted quantile are utilized to improve model performance.

The objective function of XGBoost consists of two parts: a loss function and a regularization term (Equation (3)). The objective function is optimized by a second-order Taylor expansion of the training loss and an expansion of the regularization term. The optimized objective function is shown in Equation (4). The optimized variables are left with only the weight vector w of the t-th tree. When w takes the minimum value (Equation (5)), the loss is minimized, and the objective function determines the optimal solution (Equation (6)).

$$\mathcal{L} = \sum_i l(\hat{y}_i, y_i) + \sum_k \Omega(f_k) \tag{3}$$

where $\mathcal{L}$ is the predicted value. l is a differentiable convex loss function that measures the difference between the predicted value $\hat{y}$ and the real value y_i of the i-th leaf. The second

part Ω embodies the complexity of k trees, and f_k indicates the k-th tree. The smaller the Ω value, the more generalized the model.

$$\mathcal{L}^{(t)} = \sum_{j=1}^{T}\left[G_j w_j + \frac{1}{2}\left(H_j + \lambda\right) {w_j}^2 \right] + \gamma T \tag{4}$$

where $\mathcal{L}^{(t)}$ is the predicted value of the t-th tree, T is the number of branches in the tree, and w_j is the weight value of the j-th leaf node. G_j is the cumulative sum of first-order partial derivatives of the samples contained in leaf node j, and H_j is the cumulative sum of second-order partial derivatives of the samples included in leaf node j. λ is a regularization factor greater than or equal to 0 and is used to weigh the empirical risk and model complexity. γ is a regularization coefficient of the node number of the t-th tree.

$$w_j^* = -\frac{G_j}{H_j + \lambda} \tag{5}$$

where w^*_j is the weight value of each leaf node.

$$Obj = -\frac{1}{2}\sum_{j=1}^{T}\frac{G_j^2}{H_j + \lambda} + \gamma T \tag{6}$$

where *Obj* is the final predicted value.

The EnPr model integrates the advantages of RF, ET, XGBoost, and CNN. RF, ET, and XGBoost are attributed to decision tree models, and tree models feature simple structures, good interpretation, and relatively little demand on sample amount. Neural network models are characterized by strong robustness, good self-organization and self-learning performance, accurate depiction of complex nonlinear relationships, and excellent feature synthesis capability. Thus, EnPr can achieve relatively accurate prediction of coseismic landslides over different earthquake-struck regions.

3.3. Evaluation Metrics

All the actual coseismic landslides are adopted to evaluate the prediction accuracy. The evaluation metrics include ACC (accuracy), AUC (area under curve), and ROC (receiver operating characteristic), and these three metrics are the most commonly used in prediction tasks [52]. ACC (Equation (7)) reflects the overall prediction accuracy.

$$\text{Accuracy} = \frac{\text{TP} + \text{TN}}{\text{TP} + \text{FP} + \text{TN} + \text{FN}} \tag{7}$$

where TP (true positive) indicates the count of landslide instances that are accurately forecasted, FN (false negative) indicates the count of non-landslide instances that are accurately forecasted, FP (false positive) denotes the count of non-landslide instances that are forecasted as landslide instances, and TN (true negative) means the count of landslide instances that are predicted as non-landslide instances.

AUC is the area under the ROC curve and can embody the prediction performance of a model. The AUC value ranges from 0.5 to 1, and a larger AUC value indicates better predictive ability of a model.

The ROC curve [53] is a commonly used statistical test that is a curve plotted with Sensitivity as the x-axis and 1-Specificity as the y-axis. The accuracy of a prediction model is assessed by true positive rate [54]. The closer the curve is to the upper left corner, the more accurate the model.

3.4. Gini Coefficient

The Gini coefficient in XGBoost is adopted to calculate the contribution of various influencing factors. The Gini importance depends on impurity. The larger the Gini coefficient, the higher the impurity. The Gini impurity for a node in a tree is shown in Equation (8). The Gini decrease is the sum (weighted sum) of the Gini coefficient of each node minus the Gini coefficient of its child nodes. The decrease in the Gini impurity is shown in Equation (9). Gini importance is the weighted sum of the Gini decrease of the same feature nodes on all trees. The importance of an influencing factor to ETL distribution is shown in Equation (10).

$$i(\tau) = 1 - p_1^2 - p_0^2 \tag{8}$$

where τ is a node in a tree T, and $i(\tau)$ is the Gini impurity of the node. p_0 denotes the number proportion of the samples that are judged not to be landslides at the node τ. p_1 represents the number proportion of the samples that are judged to be landslides at the node τ.

$$\Delta i(\tau) = i(\tau) - p_l i(\tau_l) - p_r i(\tau_r) \tag{9}$$

where $\Delta i(\tau)$ is the decrease in the Gini impurity. p_l and p_r are the sample subsets when the sample set is split by the left and right nodes, respectively.

$$I_G(\theta) = \sum_T \sum_\tau \Delta \mathrm{i}_\theta(\tau, T) \tag{10}$$

where I_G is the Gini importance, $\Delta \mathrm{i}_\theta$ is the decrease of feature θ in the Gini impurity, and τ is a node in a tree T. If a particular feature θ is selected more times for node segmentation, it contributes more to the overall discrimination in a prediction task. Thus, the feature θ possesses greater Gini importance and contributes more to ETL prediction.

4. Results and Discussions

4.1. Near-Real Spatial Prediction of ETLs

Figures 4 and 5 show the ETL prediction by the EnPr model for the 2017 Jiuzhaigou and 2022 Lushan earthquakes. The factual positions of all coseismic landslides are employed to validate the prediction result and accuracy, and the statistics of the prediction results are shown in Table 4. The results indicate that 82.32% of Jiuzhaigou coseismic landslides are located in the predicted high and very high probability areas, and the very high and high probability areas account for 12.2% of the study area. In total, 82.53% of Lushan ETLs fall in the predicted high and very high probability areas, and the very high and high probability regions occupy 6.18% of the study area. Table 5 and Figure 6 exhibit the prediction accuracy of the EnPr model for the Jiuzhaigou and Lushan earthquakes. The ACC and AUC values for the Jiuzhaigou earthquake reach 91.28% and 0.8534, respectively. The ACC and AUC values for the Lushan earthquake attain 93.78% and 0.8832, respectively.

Table 4. Statistics of the prediction result via the EnPr model for the Jiuzhaigou and Lushan earthquakes.

Earthquake	Probability Level	Area Proportion	Landslide Area (km^2)	Number Proportion of Landslides
Jiuzhaigou	Very low	43.13%	1.01	5.03%
	Low	38.66%	1.17	5.86%
	Medium	6.00%	1.36	6.79%

	High	6.52%	4.83	24.16%
	Very high	5.68%	11.63	58.16%
Lushan	Very low	39.81%	0.14	2.59%
	Low	48.14%	0.37	6.63%
	Medium	5.87%	0.45	8.25%
	High	3.61%	1.28	23.26%
	Very high	2.57%	3.27	59.27%

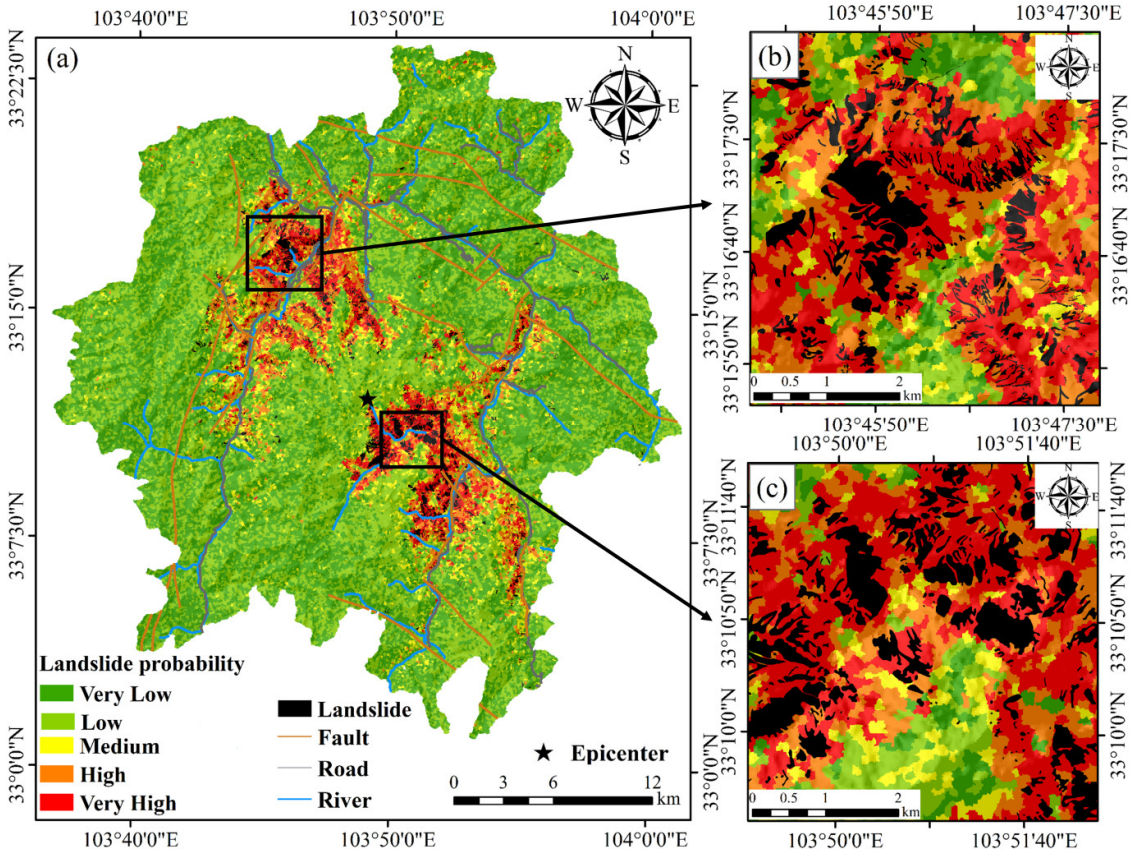

Figure 4. Spatial distribution prediction and factual location of landslides triggered by the M_S 7.0 Jiuzhaigou earthquake. (**a**) Meizoseismal region with dense coseismic landslides. (**b**) A magnified representation of the landslide-dense region in the northwest. (**c**) A magnified representation of the landslide-dense region in the southeast.

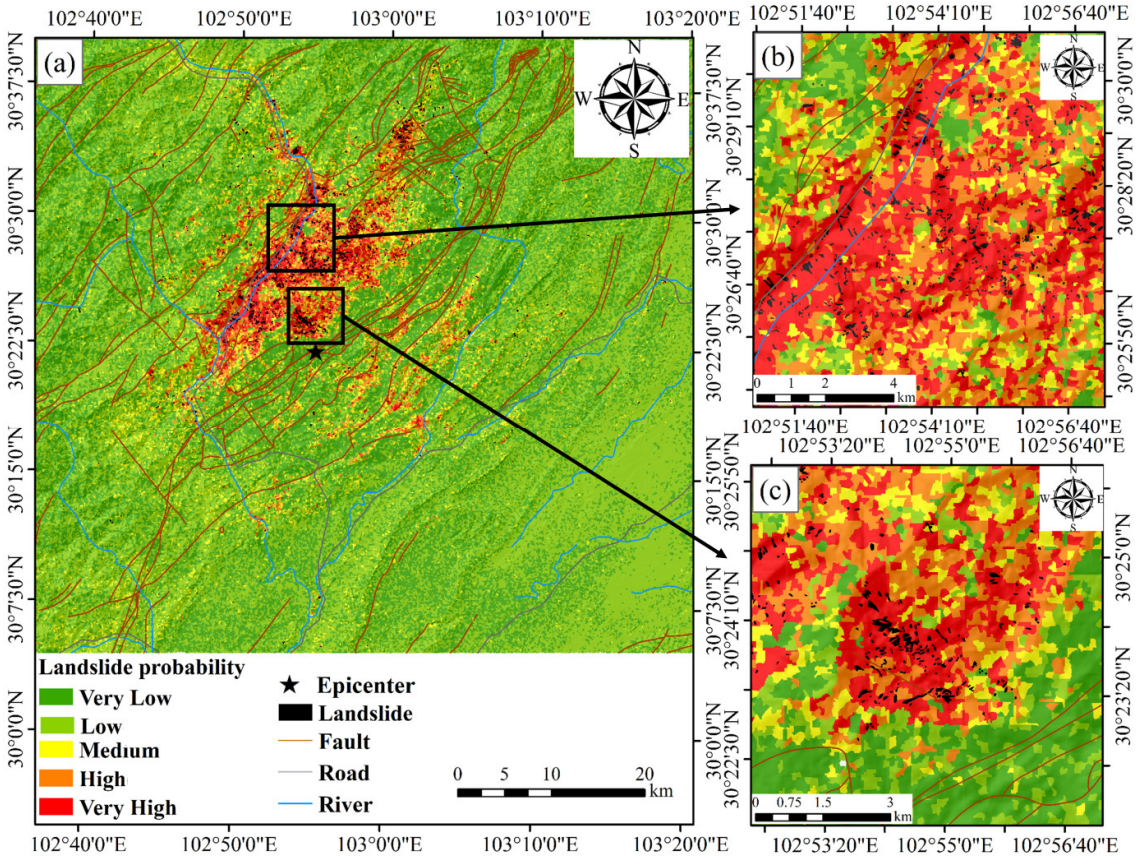

Figure 5. Spatial distribution prediction and factual location of landslides triggered by the M_S 6.1 Lushan earthquake. (**a**) Meizoseismal region with numerous coseismic landslides. (**b**) A magnified representation of the landslide-dense region in the northwest. (**c**) A magnified representation of the landslide-dense region in the southeast.

Table 5. Prediction accuracy of the EnPr model for the Jiuzhaigou and Lushan (2022) earthquakes.

Earthquake	ACC	AUC
Jiuzhaigou	91.28%	0.8534
Lushan (2022)	93.78%	0.8832

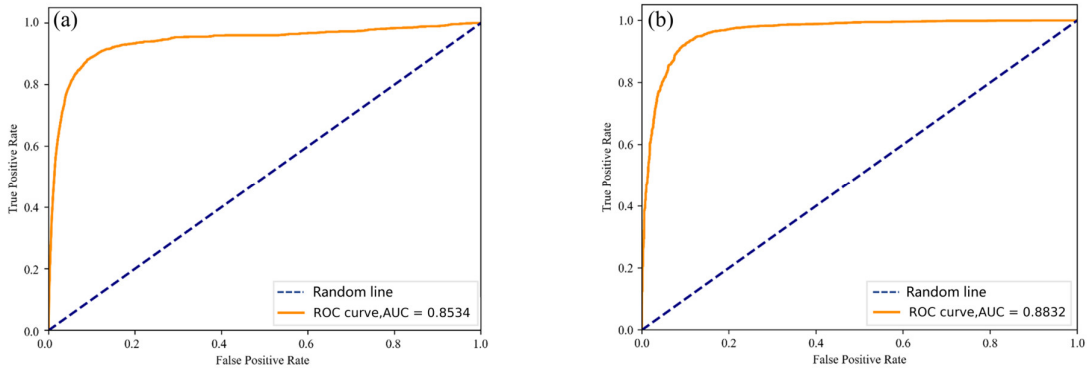

Figure 6. ROC curves and AUC precision values of coseismic landslide prediction for two newly occurring earthquakes. (**a**) Jiuzhaigou earthquake. (**b**) Lushan earthquake in 2022. The closer the ROC curve is to the upper left corner, the higher the accuracy; the closer the AUC value is to 1, the higher the accuracy.

4.2. Comparison of Model Accuracy

The prediction accuracy of the EnPr model is compared with those of five state-of-the-art models: RF, ET, XGBoost, CNN, and Transformer (Figure 7). The optimized parameter values of the five algorithms are shown in Table 6. For the Jiuzhaigou earthquake, compared with the RF, ET, XGBoost, CNN, and Transformer models, the ACC value is improved by 3.23%, 3.48%, 4.77%, 22.89%, and 27.60%, respectively. The AUC value is improved by 2.31%, 5.19%, 1.13%, 10.44%, and 19.66%, respectively. For the Lushan earthquake, the ACC value is improved by 2.18%, 1.25%, 5.68%, 6.25%, and 27.77%, respectively, and the AUC value is improved by3.32%, 2.08%, 2.55%, 12.94%, and 23.17%, respectively. Figures 8 and 9 show comparisons of the predicted distribution maps by six methods. Unlike the other five models, EnPr does not predict non-landslide regions as high or very high probability areas and well avoids false alarms. In addition, EnPr relatively exactly predicts landslide regions as very high probability areas and achieves high accuracy. Therefore, EnPr exhibits relatively accurate prediction and good generalization ability.

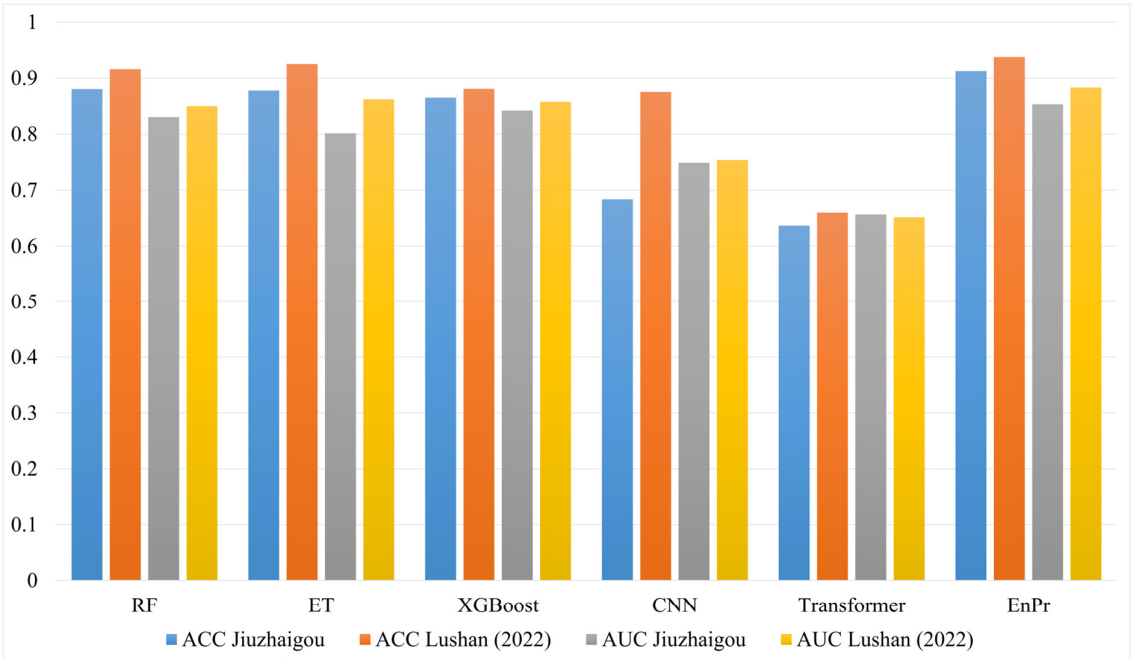

Index	Earthquake	RF	ET	XGBoost	CNN	Transformer	EnPr
ACC	Jiuzhaigou	0.8805	0.8780	0.8651	0.6839	0.6368	**0.9128**
	Lushan (2022)	0.9160	0.9253	0.881	0.8753	0.6601	**0.9378**
AUC	Jiuzhaigou	0.8303	0.8015	0.8421	0.7490	0.6568	**0.8534**
	Lushan (2022)	0.8500	0.8624	0.8577	0.7538	0.6515	**0.8832**

Figure 7. Comparison of ACC and AUC precision values among six prediction models for the Jiuzhaigou and Lushan (in 2022) earthquakes.

Table 6. Optimized parameter values in the XGBoost, RF, ET, CNN, and Transformer algorithms. Colsample_bytree is used to control the feature sampling rate when constructing each tree. Subsample controls the sampling rate of training data in each tree. Min_samples_split determines the minimum number of samples required for feature segmentation. Min_samples_leaf means the minimum number of samples required for each leaf node. Max_features controls the maximum number of features when building a tree.

XGBoost	Parameter	Estimator Number	Colsample_Bytree	Learning Rate	Maximum Depth	Subsample
	Optimized value	100	0.9	0.3	9	0.9
RF	Parameter	Estimator number	Criterion	Min_samples_split	Min_samples_leaf	Max_features
	Optimized value	100	Gini	50	1	sqrt
ET	Parameter	Estimator number	Criterion	Max_features	—	—
	Optimized value	5	Entropy	5	—	—
CNN	Parameter	Epoch	Verbose	Activation	—	—
	Optimized value	200	2	Tanh	—	—
Transformer	Parameter	Epoch	Learning rate	—	—	—
	Optimized value	300	0.001	—	—	—

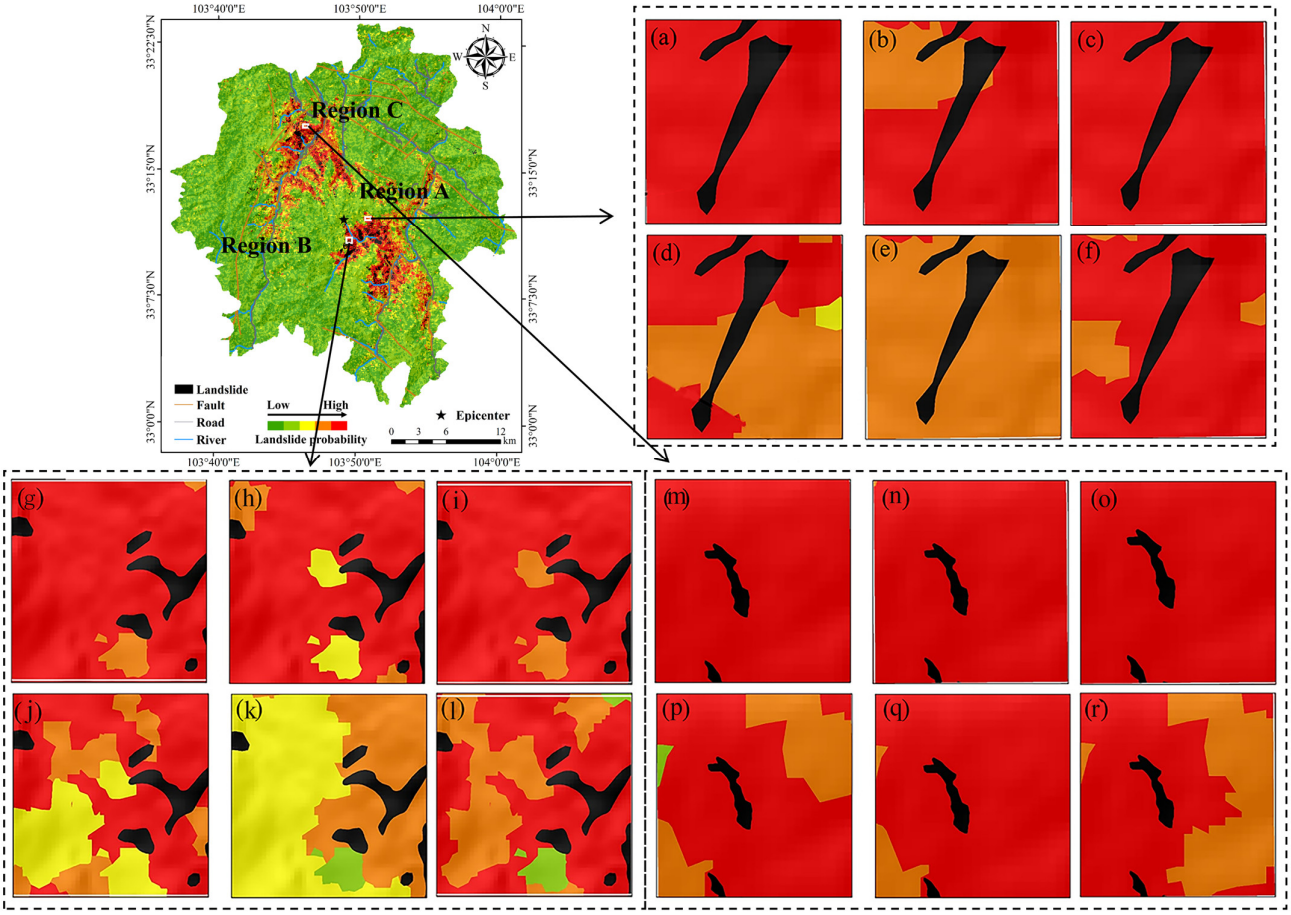

Figure 8. Comparison of the predicted distribution maps among six models for the Jiuzhaigou earthquake. Regions A, B, and C are randomly selected from the whole study area for exhibition. (**a**,**g**,**m**) RF. (**b**,**h**,**n**) ET. (**c**,**i**,**o**) XGBoost. (**d**,**j**,**p**) CNN. (**e**,**k**,**q**) Transformer. (**f**,**l**,**r**) EnPr.

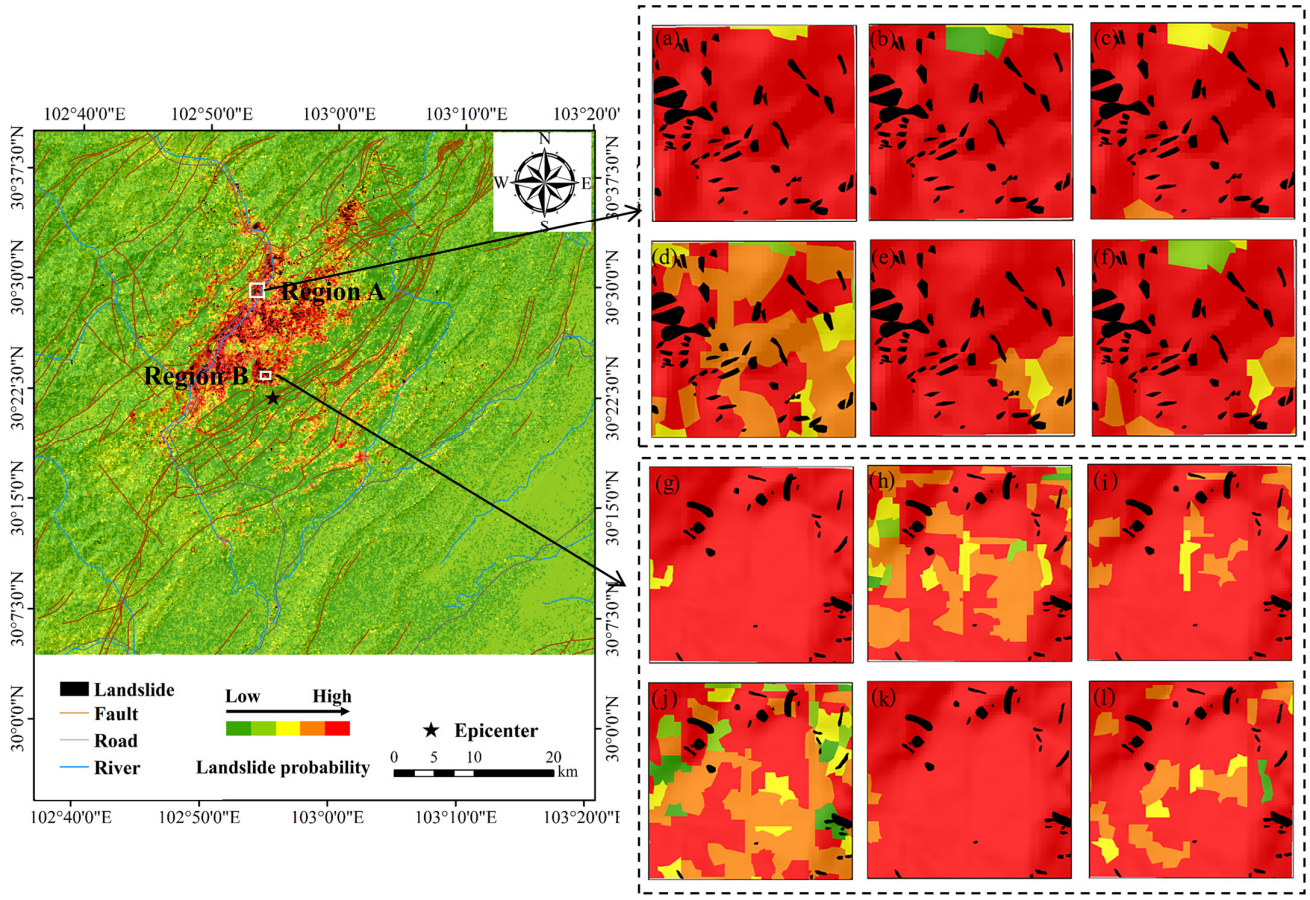

Figure 9. Comparison of the predicted distribution maps among six models for the Lushan (in 2022) earthquake. Regions A and B are randomly selected from the whole study area for presentation. (**a**,**g**) RF. (**b**,**h**) ET. (**c**,**i**) XGBoost. (**d**,**j**) CNN. (**e**,**k**) Transformer. (**f**,**l**) EnPr.

4.3. Significant Factors Influencing Coseismic Landslide Distribution

Figure 10 shows the Gini importance of each influencing factor. The factors of MMI, elevation, distance to fault, slope angle, and distance to road are the main factors affecting the spatial distribution of coseismic landslides. Moreover, the actual ETL distribution of a series of great earthquakes in the Tibetan Plateau also indicates the same critical influencing factors (Figure 11). In the southeast of the Tibetan Plateau, coseismic landslides usually occur in the areas with large MMI values (VI~VIII), medium to high elevations (600~4500 m), steep relief (20°~60°), dense faults, or developed road networks. Therefore, seismic intensity, high and steep terrain, pre-earthquake fault tectonics, and pre-seismic road construction have important controlling or inducing effects on the occurrence of coseismic landslides.

(1) Regarding seismic intensity, slope surfaces are inclined to be destructed by strong ground motion due to great shear strain. In addition, a great seismic intensity causes excess pore water pressure rising rapidly within a slope, and then the soil mass becomes liquefied and flows down [41]. Therefore, coseismic landslides densely occur over the regions with great seismic intensity.

(2) With regard to the topographic action, coseismic landslides are generally shallow landslides [55] and mostly located along the high ridges [56]. That is attributed to the enhanced ground motion at the top of mountains [36,57]. High and steep topography increases gravitational instability and amplifies the seismic wavefield [36]. The acceleration amplification factors on the ground surface behind the crest typically exhibit

a high degree of variability around a value of 1. The impact of topography on ground motion amplification diminishes notably as the distance from the crest increases, approaching zero near the free-field boundary [58]. In slope angle, the amplification factor reaches a maximum when the slope angle is 32.3° [58]. When the slope angle is greater than 32.3°, a secondary peak appears in the amplification factor curve as the slope angle increases. The biggest amplification does not always happen at the crest; rather, it is often observed below the crest. [58]. In slope elevation, when the wavelength is smaller than the slope height, it has no impact on the distribution of the maximum amplification factor. The ratio of slope height to wavelength has a significant effect not only on the amplification magnitude but also on the location of the maximum amplification. As the number of cycles increases, the amplification value increases, and a secondary peak occurs in the acceleration amplification curve [58]. Hence, the impact of slope topography on ground acceleration amplification is intricate, and the ratio between wavelength and slope size plays a significant role.

(3) Regarding pre-seismic fault tectonics, active faults lead to gradual deformation of surrounding slope materials and decrease the stability of rock and soil mass due to developed horizontal and vertical large cracks. The slope materials near faults are characterized by fractured structure, reduced shear strength, and relatively poor stability [59]. Thus, the distribution of coseismic landslides is closely relevant to the pre-earthquake fault movements.

(4) Pre-earthquake road construction is accompanied by slope excavation and artificial explosion that obviously damage the natural stress state of slopes [42]. The back pressure in a slope foot significantly decreases to release stress, and the upper slope poses plastic extrusion to the excavated free surfaces. Thus, the free surfaces gradually become unstable, and the weak intercalation forms [42]. Artificial explosion generates new cracks, opens pre-existing fissures, and further reduces slope stability [42]. Therefore, slopes in the vicinity of roads have suffered from a destruction of natural stress balance and are apt to lose stability under a great earthquake.

5. Conclusions

Near-real spatial prediction of coseismic landslides can rapidly predict the location of hundreds of thousands of coseismic landslides shortly after a violent earthquake; thus, it can strongly support effective and efficient emergency rescue. This work focuses on six great earthquakes occurring on the southeastern margin of the Tibetan Plateau from 2008 to 2022 and proposes a novel ensemble learning model of EnPr to realize near-real prediction of ETLs. The model combines the advantages of tree-structured models and a neural network and features relatively good generalization and relatively accurate prediction ability. Moreover, this work reveals the critical factors affecting the distribution of coseismic landslides. Since the multi-source data used in this work are publicly available on a global scale, the suggested EnPr model can be applied to new large earthquakes in the future.

(1) The EnPr model is applied to the ETL prediction of two newly occurring earthquakes. Validated by all the actual coseismic landslides, the ACC values for the Jiuzhaigou and Lushan earthquakes reach 91.28% and 93.78%, respectively. The AUC values for the Jiuzhaigou and Lushan earthquakes attain 0.85 and 0.88, respectively. Moreover, the EnPr model outperforms five state-of-the-art machine learning or deep learning models: RF, ET, XGBoost, CNN, and Transformer. For the Jiuzhaigou earthquake, compared with the RF, ET, XGBoost, CNN, and Transformer models, the ACC value is improved by 3.23%, 3.48%, 4.77%, 22.89%, and 27.60%, respectively. The AUC value is improved by 2.31%, 5.19%, 1.13%, 10.44%, and 19.66%, respectively. For the Lushan earthquake, the ACC value is improved by 2.18%, 1.25%, 5.68%, 6.25%, and 27.77%, respectively, and the AUC value is improved by 3.32%, 2.08%, 2.55%, 12.94%,

and 23.17%, respectively. Therefore, EnPr features relatively accurate prediction ability.

(2) Seismic intensity, high and steep topography, pre-seismic fault tectonics, and pre-earthquake road construction have important controlling or triggering influences on coseismic landslide occurrence. Great seismic intensity causes severe damage to rock and soil mass and a dramatic increase in excess pore water pressure. So coseismic landslides are concentrated in the regions with great seismic intensities. High and steep relief has an amplified effect on the refraction and reflection of seismic waves; thus, coseismic landslides densely occur on thin ridges and steep mountains. Pre-earthquake fault movement indicates the development of large cracks and the fracture of rock and soil mass before an earthquake, so coseismic landslides primarily occur in the fault-developed regions. Pre-seismic road construction excavates slope feet and destroys the intactness of rock and soil mass, and the natural stress and seepage fields are destructed. Therefore, numerous coseismic landslides are distributed along two sides of roads.

In our future work, we will explore the integration of the short-term probability of mechanical rock failure following severe ground shaking to enhance the precision of near-real-time prediction of ETLs. Additionally, we aim to develop an early warning platform to extend the prediction of earthquake-induced landslides to more regions.

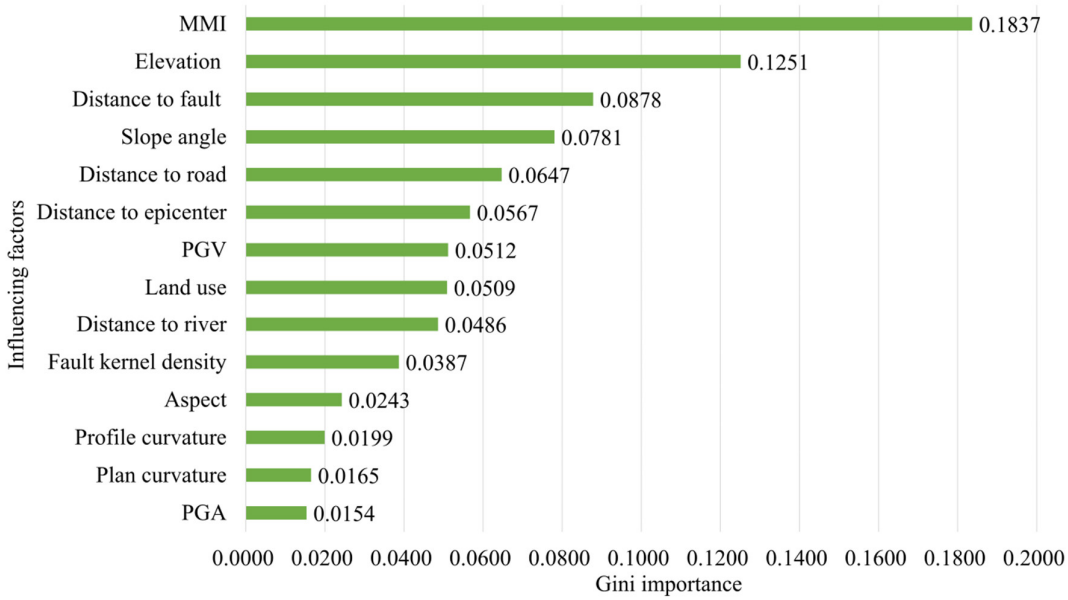

Figure 10. Contribution of different influencing factors to coseismic landslide occurrence. PGV: peak ground velocity; PGA: peak ground acceleration; MMI: modified Mercalli intensity.

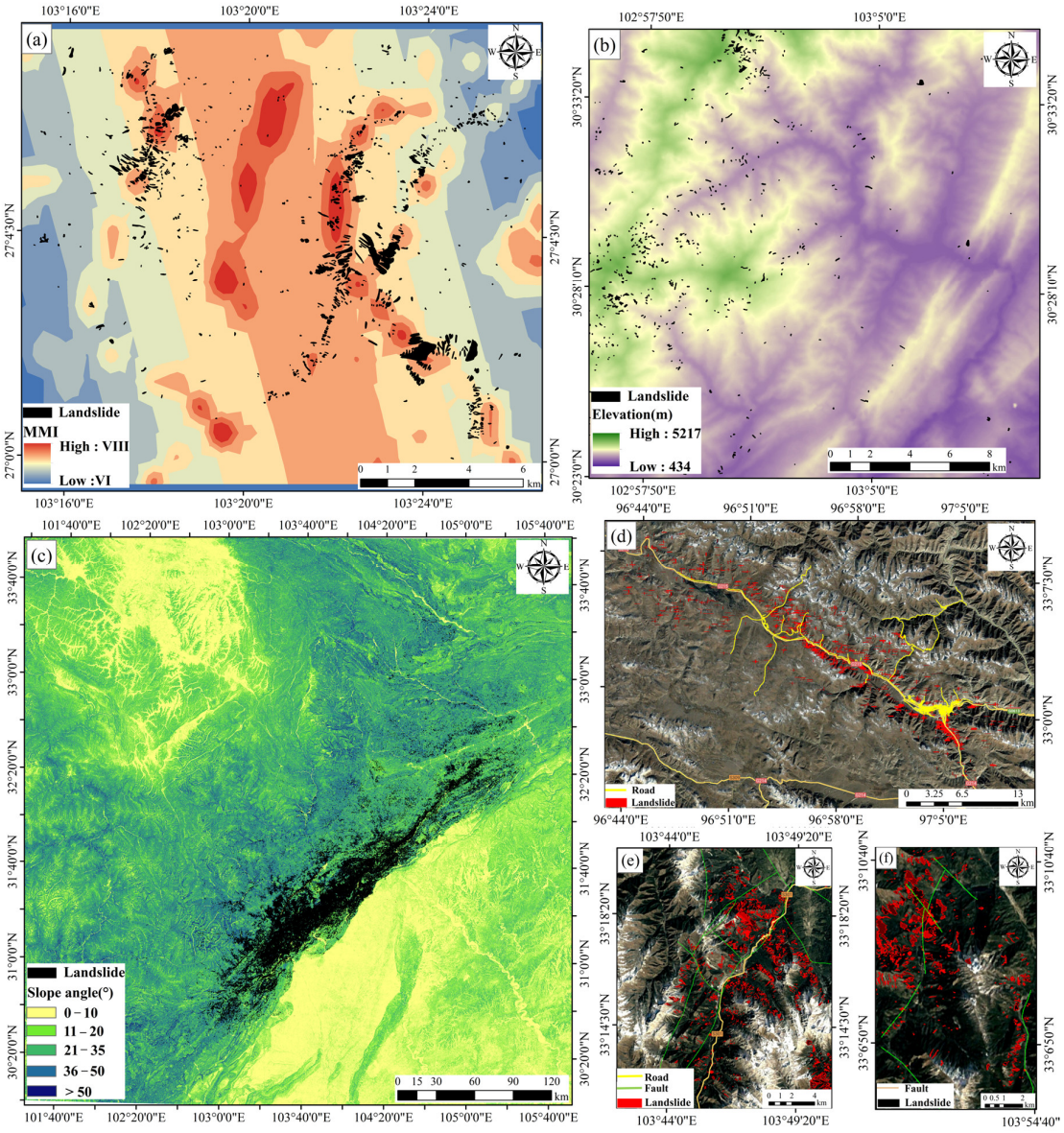

Figure 11. Distribution characteristics of landslides triggered by earthquakes. (**a**) Distribution of coseismic landslides with different MMI values in the 2014 Ludian earthquake. (**b**) Distribution characteristics of coseismic landslides with different elevation in the 2013 Lushan earthquake region. (**c**) Distribution of coseismic landslides with different slope angle in the 2008 Wenchuan earthquake area. (**d**) Distribution of coseismic landslides near the roads in the 2010 Yushu earthquake region. (**e**,**f**) Distribution of coseismic landslides near the faults in the northwest and southeast of the 2017 Jiuzhaigou earthquake area.

Author Contributions: Conceptualization, A.Z. and X.W.; methodology, A.Z. and X.W.; software, A.Z.; validation, A.Z.; formal analysis, A.Z. and X.W.; data curation, A.Z.; writing—original draft preparation, A.Z., X.W. and C.X.; writing—review and editing, A.Z., X.W., Q.Y., H.G. and D.L. All authors have read and agreed to the published version of the manuscript.

Funding: This work is funded by the National Natural Science Foundation of China (42311530065, U21A2013, 72074198, 71874165), Natural Social Science Foundation of China (23AZD072), Opening Fund of Key Laboratory of Geological Survey and Evaluation of Ministry of Education (Grant Nos. GLAB2020ZR02, GLAB2022ZR02), State Key Laboratory of Biogeology and Environmental Geology

(Grant No. GBL12107), the Fundamental Research Funds for the Central Universities, China University of Geosciences (Wuhan) (CUG2642022006), and Hunan Provincial Natural Science Foundation of China (2021JC0009).

Data Availability Statement: All data are available within this article.

Conflicts of Interest: The authors declare no conflicts of interest.

References

1. Tanyas, H.; Rossi, M.; Alvioli, M.; van Westen, C.J.; Marchesini, I. A Global Slope Unit-Based Method for the Near Real-Time Prediction of Earthquake-Induced Landslides. *Geomorphology* **2019**, *327*, 126–146. https://doi.org/10.1016/j.geomorph.2018.10.022.
2. Xu, C.; Xu, X.; Yao, X.; Dai, F. Three (nearly) complete inventories of landslides triggered by the May 12, 2008 Wenchuan Mw 7.9 earthquake of China and their spatial distribution statistical analysis. *Landslides* **2014**, *11*, 441–461. https://doi.org/10.1007/s10346-013-0404-6.
3. Karagianni, A.; Lazos, I.; Chatzipetros, A. *Remote Sensing Techniques in Disaster Management: Amynteon Mine Landslides, Greece*; Lecture Notes in Geoinformation and Cartography; Springer: Cham, Switzerland, 2019; pp. 209–235. https://doi.org/10.1007/978-3-030-05330-7_9.
4. Huang, Y.; Xie, C.; Li, T.; Xu, C.; He, X.; Shao, X.; Xu, X.; Zhan, T.; Chen, Z. An open-accessed inventory of landslides triggered by the Ms 6.8 Luding earthquake, China on 5 September 2022. *Earthq. Res. Adv.* **2022**, *3*, 100181. https://doi.org/10.1016/j.eqrea.2022.100181.
5. Wang, L.; Zuo, B.; Le, Y.; Chen, Y.; Li, J. Penetrating remote sensing: Next-generation remote sensing for transparent earth. *The Innovation.* **2023**, *4*, 100519. https://doi.org/10.1016/j.xinn.2023.100519.
6. Jones, J.N.; Boulton, S.J.; Stokes, M.; Bennett, G.L.; Whitworth, M.R. 30-year record of Himalaya mass-wasting reveals landscape perturbations by extreme events. *Nat. Commun.* **2021**, *12*, 6701. https://doi.org/10.1038/s41467-021-26964-8.
7. Roback, K.; Clark, M.K.; West, A.J.; Zekkos, D.; Li, G.; Gallen, S.F.; Champlain, D.; Godt, J.W. *Map Data of Landslides Triggered by the 25 April 2015 Mw 7.8 Gorkha, Nepal Earthquake*; U.S. Geological Survey Data Release; Landslide Hazards Program: Reston, VA, USA, 2017. https://doi.org/10.5066/F7DZ06F9.
8. Newmark, N.M. Effects of Earthquakes on Dams and Embankments. *Géotechnique* **1965**, *15*, 139–160. https://doi.org/10.1680/geot.1965.15.2.139.
9. Jibson, R.W.; Harp, E.L.; Michael, J.A. A method for producing digital probabilistic seismic landslide hazard maps. *Eng. Geol.* **2000**, *58*, 271–289. https://doi.org/10.1016/S0013-7952(00)00039-9.
10. Godt, J.W.; Sener, B.; Verdin, K.L.; Wald, D.J.; Earle, P.S.; Harp, E.L.; Jibson, R.W. *Rapid Assessment of Earthquake-Induced Landsliding*; Association for Disaster Prevention Research: Tokyo, Japan, 2008; pp. 219–222.
11. Cheng, Q.; Tian, Y.; Lu, X.; Huang, Y.; Ye, L. Near-real-time Prompt Assessment for Regional Earthquake Induced Landslides Using Recorded Ground Motions. *Comput. Geosci.* **2021**, *149*, 104709. https://doi.org/10.1016/j.cageo.2021.104709.
12. Nowicki Jessee, M.A.; Hamburger, M.W.; Allstadt, K.; Wald, D.J.; Robeson, S.M.; Tanyas, H.; Hearne, M.; Thompson, E.M. A Global Empirical Model for Near-Real-Time Assessment of Seismically Induced Landslides. *J. Geophys. Res. Earth Surf.* **2018**, *123*, 1835–1859. https://doi.org/10.1029/2017JF004494.
13. Kritikos, T.; Robinson, T.R.; Davies, T.R.H. Regional coseismic landslide hazard assessment without historical landslide inventories: A new approach. *J. Geophys. Res. Earth Surf.* **2015**, *120*, 711–729. https://doi.org/10.1002/2014JF003224.
14. Robinson, T.R.; Rosser, N.J.; Davies, T.R.H.; Wilson, T.M.; Orchiston, C. Near-realtime modeling of landslide impacts to inform rapid response: An example from the 2016 Kaikoura, New Zealand, earthquake. *Bull. Seism. Soc. Am.* **2018**, *108*, 1665–1682. https://doi.org/10.1785/0120170234.
15. Robinson, T.R.; Rosser, N.J.; Densmore, A.L.; Williams, J.G.; Kincey, M.E.; Benjamin, J.; Bell, H.J.A. Rapid post-earthquake modelling of coseismic landslide magnitude and distribution for emergency response decision support. *Nat. Hazards Earth Syst. Sci.* **2017**. https://doi.org/10.5194/nhess-2017-83.
16. Parker, R.N.; Rosser, N.J.; Hales, T.C. Spatial prediction of earthquake-induced landslide probability. *Nat. Hazards Earth Syst. Sci.* **2017**. https://doi.org/10.5194/nhess-2017-193.
17. Nowicki, M.A.; Wald, D.J.; Hamburger, M.W.; Hearne, M.; Thompson, E.M. Development of a Globally Applicable Model for Near Real-Time Prediction of Seismically Induced Landslides. *Eng. Geol.* **2014**, *173*, 54–65. https://doi.org/10.1016/j.enggeo.2014.02.002.
18. He, Q.; Wang, M.; Liu, K. Rapidly Assessing Earthquake-Induced Landslide Susceptibility on a Global Scale Using Random Forest. *Geomorphology* **2021**, *391*, 107889. https://doi.org/10.1016/j.geomorph.2021.107889.
19. Gallen, S.F.; Clark, M.K.; Godt, J.W. Coseismic landslides reveal near-surface rock strength in a high-relief, tectonically active setting. *Geology* **2015**, *43*, 11–14. https://doi.org/10.1130/G36080.1.
20. Fan, X.M.; Fang, C.Y.; Dai, L.X.; Wang, X.; Luo, Y.; Wei, T.; Wang, Y. Near Real-Time Prediction of Spatial Distribution Probability of Earthquake-Induced Landslides—Take the Lushan Earthquake on June 1, 2022 as an Example. *J. Eng. Geol.* **2022**, *30*, 729–739. https://doi.org/10.13544/j.cnki.jeg.2022−0665.

21. Xu, X.; Tan, X.; Yu, G.; Wu, G.; Fang, W.; Chen, J.; Shen, J. Normal- and Oblique-Slip of the 2008 Yutian Earthquake: Evidence for Eastward Block Motion, Northern Tibetan Plateau. *Tectonophysics* **2013**, *584*, 152–165. https://doi.org/10.1016/j.tecto.2012.08.007.
22. Xu, X.; Xu, C.; Yu, G.; Wu, X.; Li, X.; Zhang, J. Primary surface ruptures of the Ludian M_w 6.2 Earthquake, southeastern Tibetan Plateau, China. *Seismol. Res. Lett.* **2015**, *86*, 1622–1635.
23. Xu, C.; Xu, X.; Shen, L.; Dou, S.; Wu, S.; Tian, Y.; Li, X. Inventory of Landslides Triggered by the 2014 Ms 6.5 Ludian Earthquake and its Implications on Several Earthquake Parameters. *Seismol. Geol.* **2014**, *36*, 1186–1203. https://doi.org/10.3969/j.issn.0253−4967.2014.04.020.
24. Wang, X.; Mao, H. Spatio-temporal Evolution of Post-Seismic Landslides and Debris Flows: 2017 Ms 7.0 Jiuzhaigou Earthquake. *Environ. Sci. Pollut. Res.* **2022**, *29*, 15681–15702. https://doi.org/10.1007/s11356-021-16789-9.
25. Shao, X.; Xu, C.; Ma, S. Preliminary Analysis of Coseismic Landslides Induced by the 1 June 2022 MS 6.1 Lushan Earthquake, China. *Sustainability* **2022**, *14*, 16554. https://doi.org/10.3390/su142416554.
26. England, P.; Molnar, P. Active deformation of Asia: From kinematics to dynamics. *Science* **1997**, *278*, 647–650. https://doi.org/10.1126/science.278.5338.647.
27. Molnar, P.; Tapponnier, P. Cenozoic tectonics of Asia: Effects of a continental collision. *Science* **1975**, *189*, 419–426. https://doi.org/10.1126/science.189.4201.419.
28. Wang, Y.; Wang, Y.; Zhang, P.; Zhang, J.; Zhang, B.; Liu-Zeng, J.; Zhou, R.; Wang, W.; Zhang, H.; Li, Z. Cenozoic tectonic evolution of regional fault systems in the SE Tibetan Plateau. *Sci. China Earth Sci.* **2022**, *65*, 601–623. https://doi.org/10.1007/s11430-021-9880-3.
29. Xu, X.W.; Chen, G.H.; Wang, Q.X.; Cen, L.C.; Ren, Z.K.; Xu, C.; Shi, F. Discussion on Seismogenic Structure of Jiuzhaigou Earthquake and its Implication for Current Strain State in the Southeastern Qinghai Tibet Plateau. *Chin. J. Geophys.* **2017**, *60*, 4018–4026. https://doi.org/10.6038/cjg20171028.
30. Xu, C.; Xu, X.; Yu, G. Landslides Triggered by Slipping-Fault-Generated Earthquake on a Plateau: An Example of the 14 April 2010, Ms 7.1, Yushu, China Earthquake. *Landslides* **2013**,10, 421–431. https://doi.org/10.1007/s10346-012-0340-x.
31. Liu-Zeng, J.; Tapponnier, P.; Gaudemer, Y.; Ding, L. Quantifying Landscape Differences across the Tibetan Plateau: Implications for Topographic Relief Evolution. *J. Geophys. Res.* **2008**, *113*, F04018. https://doi.org/10.1029/2007JF000897.
32. Wang, J.; Li, N.; Stuart, F.M.; Nicola, L.D.; Zhang, H.; Wang, Y.; Pang, J.; Zhao, Y. Rapid Exhumation Processes of the Gaoligong Mountain Range in the Southeastern Margin of the Qinghai–Tibet Plateau Since the Late Cenozoic. *Front. Earth Sci.* **2022**, *10*, 875237. https://doi.org/10.3389/feart.2022.875237.
33. Styron, R.; Pagani, M. The GEM Global Active Faults Database. *Earthq. Spectra* **2020**, *36*, 160–180. https://doi.org/10.1177/8755293020944.
34. Wang, L. *Fault Distribution Data of Sichuan Tibet Traffic Corridor (2020)*; National Tibetan Plateau Data Center: Beijing, China, 2021. https://doi.org/10.11888/Geo.tpdc.271624.
35. Li, Y.S.; Huang, C.; Yi, S.J.; Wu, C.H. Study on seismic fault and source rupture tectonic dynamic mechanism of Jiuzhaigou Ms 7.0 earthquake. *J. Eng. Geol.* **2017**, *25*, 1141–1150. https://doi.org/10.13544/j.cnki.jeg.2017.04.029.
36. Huang, M.W.; Chen, C.Y.; Wu, T.H.; Chang, C.L.; Liu, S.Y.; Kao, C.Y. GIS-based evaluation on the fault motion-induced coseismic landslides. *J. Mt. Sci.* **2012**, *9*, 601–612. https://doi.org/10.1007/s11629-012-2434-2.
37. Wang, L.; Wu, Z.; Xia, K.; Liu, K.; Wang, P.; Pu, X.; Li, L. Amplification of Thickness and Topography of Loess Deposit on Seismic Ground Motion and its Seismic Design Methods. *Soil Dyn. Earthq. Eng.* **2019**, *126*, 105090. https://doi.org/10.1016/j.soildyn.2018.02.021.
38. Keefer, D.K. Statistical analysis of an earthquake-induced landslide distribution—The 1989 Loma Prieta, California event. *Eng. Geol.* **2000**, *58*, 231–249. https://doi.org/10.1016/S0013-7952(00)00037-5.
39. Dunham, A.M.; Kiser, E.; Kargel, J.S.; Haritashya, U.K.; Watson, C.S.; Shugar, D.H.; Hughes, A.; DeCelles, P.G. Topographic Control on Ground Motions and Landslides From the 2015 Gorkha Earthquake. *Geophys. Res. Lett.* **2022**, 49, e2022GL098582. https://doi.org/10.1029/2022GL098582.
40. Zhao, B. Climatological and geological controls on seismic earthflows in coastal areas. *Catena* **2024**, *235*, 107692. https://doi.org/10.1016/j.catena.2023.107692.
41. Deng, Y.; Zhao, Z.; Peng, X. Influence of Earthquake on Deformation and Stability of a Certain Landslide. In Proceedings of the 2015 4th International Conference on Sustainable Energy and Environmental Engineering, Online, 1 April 2016; pp. 226–229. https://doi.org/10.2991/icseee-15.2016.39.
42. Li, S.; Zhang, Y.; Wang, Z.; Li, L. Mapping Human Influence Intensity in the Tibetan Plateau for Conservation of Ecological Service Functions. *Ecosyst. Serv.* **2018**, *30*, 276–286. https://doi.org/10.1016/j.ecoser.2017.10.003.
43. Chi, M.; Li, Q.; Cao, Z.; Fang, J.; Wu, B.; Zhang, Y.; Wei, S.; Liu, X.; Yang, Y. Evaluation of water resources carrying capacity in ecologically fragile mining areas under the influence of underground reservoirs in coal mines. *J. Clean. Prod.* **2022**, *379*, 134449. https://doi.org/10.1016/j.jclepro.2022.134449.
44. Castillo, G.; Brereton, D. Large-scale mining, spatial mobility, place-making and development in the Peruvian Andes. *Sustain. Dev.* **2018**, *26*, 461–470. https://doi.org/10.1002/sd.1891.
45. Hilson, G. Why is there a large-scale mining 'bias' in sub-Saharan Africa? *Land Use Policy* **2019**, *81*, 852–861. https://doi.org/10.1016/j.landusepol.2017.02.013.
46. Breiman, L. Random Forests. *Mach. Learn.* **2001**, *45*, 5–32. https://doi.org/10.1023/A:1010933404324.

47. Pal, M. Random Forest Classifier for Remote Sensing Classification. *Int. J. Remote Sens.* **2005**, *26*, 217–222. https://doi.org/10.1080/01431160412331269698.
48. Fang, Z.; Wang, Y.; Peng, L.; Hong, H. Integration of Convolutional Neural Network and Conventional Machine Learning Classifiers for Landslide Susceptibility Mapping. *Comput. Geosci.* **2020**, *139*, 104470. https://doi.org/10.1016/j.cageo.2020.104470.
49. Geurts, P.; Ernst, D.; Wehenkel, L. Extremely randomized trees. *Mach. Learn.* **2006**, *63*, 3–42. https://doi.org/10.1007/s10994-006-6226-1.
50. Lecun, Y.; Bottou, L.; Bengio, Y.; Haffner, P. Gradient-based learning applied to document recognition. *Proc. IEEE* **1998**, *86*, 2278–2324. https://doi.org/10.1109/5.726791.
51. Chen, T.; Guestrin, C. Xgboost: A Scalable Tree Boosting System. In Proceedings of the 22nd ACM SIGKDD International Conference on Knowledge Discovery and Data Mining, San Francisco, CA, USA, 13–17 August 2016.
52. Mokhtari, M.; Abedian, S. Spatial prediction of landslide susceptibility in Taleghan basin, Iran. *Stoch. Environ. Res. Risk Assess.* **2019**, *33*, 1297–1325. https://doi.org/10.1007/s00477-019-01696-w.
53. Mandrekar, J.N. Receiver operating characteristic curve in diagnostic test assessment. *J. Thorac. Oncol.* **2010**, *5*, 1315–1316. https://doi.org/10.1097/ JTO.0b013e3181ec173d.
54. Fadhillah, M.F.; Achmad, A.R.; Lee, C.W. Integration of insar time-series data and GIS to assess land subsidence along subway lines in the Seoul metropolitan area, South Korea. *Remote Sens.* **2020**, *12*, 3505. https://doi.org/10.3390/rs12213505.
55. Harp, E.L.; Jibson, R.W. Landslides triggered by the 1994 Northridge, California, earthquake. *Bull. Seismol. Soc. Am.***1996**, *86*, S319–S332. https://doi.org/10.1785/BSSA08601BS319.
56. Weissel, K.W.; Stark, C.P.; Hovius, N. Landslides triggered by the 1999 Mw7.6 Chi-Chi earthquake in Taiwan and their relationship to topography. In Proceedings of the International Geoscience and Remote Sensing Symposium (IGARSS), Sydney, Australia, 9–13 July 2001; pp. 759–761.
57. Yin, Y.; Zheng, W.; Li, X.; Sun, P.; Li, B. Catastrophic landslides associated with the M8.0 Wenchuan earthquake. *Bull. Eng. Geol. Environ.* **2011**, *70*, 15–32. https://doi.org/10.1007/s10064-010-0334-7.
58. Zhang, Z.; Fleurisson, J.-A.; Pellet, F. The effects of slope topography on acceleration amplification and interaction between slope topography and seismic input motion. *Soil Dyn. Earthq. Eng.* **2018**, *113*, 420–431. https://doi.org/10.1016/j.soildyn.2018.06.019.
59. Ehteshami-Moinabadi, M.; Nasiri, S. Geometrical and structural setting of landslide dams of the Central Alborz: A link between earthquakes and landslide damming. *Bull. Eng. Geol. Environ.* **2019**, *78*, 69–88. https://doi.org/10.1007/s10064-017-1021-8.